International Journal of Engineering

Journal Homepage: www.ije.ir

# Numerical Meshless Method in Conjunction with Bayesian Theorem for Electrical Tomography of Concrete

N. Taghizadieh*, S. Movahedi

*Faculty of Civil Engineering, University of Tabriz, Tabriz, Iran*

*PAPER INFO*

*Paper history:*
Received 20 October 2019
Received in revised form 18 Decmber 2019
Accepted 16 January 2020

*Keywords*:
*Bayesian Theorem*
*Concrete*
*Electrical Tomography*
*Meshless Method*

*ABSTRACT*

Electric potential measurement technique (tomography) was introduced as a nondestructive method to evaluate concrete properties and durability. In this study, numerical meshless method was developed to solve a differential equation which simulates electric potential distribution for concrete with inclusion in two dimensions. Therefore, concrete samples with iron block inclusion in different locations were cast. Then, via a pair of electrodes attached to the samples, DC current was injected into concrete and electric potential was measured through 14 electrodes placed in the perimeter of the samples. In total, 35 different pair electrode configurations were planned for current injection. Bayesian theorem was employed to perform probabilistic tomography as well as to calculate the optimal shape coefficient in the numerical meshless method. Results of this study indicated that shape coefficient in multiquadratic radial-based function (MQ-RBF) model does significantly depend on boundary conditions. Furthermore, when the main current line is long, distribution of random variables $c$ and $\boldsymbol{e}$ fits well with normal distribution, which is in agreement with the study assumption. Also, results reveal that probabilistic tomography is more precise than deterministic tomography even without using *prior* functions. Experimental results showed that MQ-RBF model has good performance in electrical tomography. This is due to uncertainty of concrete physical properties in real conditions which can be resolved by meshless method using optimization of shape coefficient.

***doi***: *10.5829/ije.2020.33.06c.04*

## 1. INTRODUCTION

Reinforced or plain concrete has been used for decades in many countries. However, these structures are gradually being deteriorated and need inspection for early rehabilitation or repair [1]. Accordingly, proper non-destructive techniques need to be developed and applied. Present techniques provide information about concrete strength [2], the position, size and orientation of inclusions like bar and fiber, condition of corrosion [3], state of humidity and probable corrosive ions, and the degree of cracking in concrete.

Various non-destructive techniques are currently used to monitor the safety and condition of construction and material like concrete structures without causing damage. They include acoustic emission, ultrasonic methods, image-based methods, x-ray tomography, laser methods [4], and electrically-based methods. Electrical methods are generally attractive since they can be performed rapidly and are relatively inexpensive.

Electrical inspection methods, which are easy to manipulate, are applied for large structures, for which there may not be ease of direct access. According to a number of studies mentioned below, some attributes of concrete can be detected via electrical measurements.

Electrical resistance measurement –using both alternate and direct currents (AC and DC)– have been applied in some studies. Despite their advantages, one of the major problems with DC methods is the measurement error produced by polarization of the specimen. Polarization is the separation of negative and positive ions trapped within the cement pores; as ions separate, less current is carried which results in a reduction in the conductivity measurement [5]. In AC methods, frequency should be kept as low as possible to avoid inductance effects owing to the long cables connecting

*Corresponding Author Email: *ntaghiza@tabrizu.ac.ir* (N. Taghizadieh)

Please cite this article as: N. Taghizadieh, S. Movahedi, Numerical Meshless Method in Conjunction with Bayesian Theorem for Electrical Tomography of Concrete, International Journal of Engineering (IJE), IJE TRANSACTIONS C: Aspects Vol. 33, No. 6, (June 2020) 1070-1084

electrodes to the ERT measurement device, and on the other hand, the frequency has to be high enough to avoid electrode polarization effects. Electrical Impedance Spectroscopy (EIS) based on AC has been utilized for detecting fiber orientations [6], fiber distributions [7], corrosion rate of reinforcing bars [8], and detection of cracks [9]. DC electrical measurements have been applied to monitor strain and crack in cement-based materials and fiber reinforced cement-based materials [10]. Although EIS and DC electrical measurements can give information about the presence of fibers and cracks, they are unable to model geometry of target accurately.

In Electrical Resistance Tomography (ERT), the spatial variations of the conductivity is reconstructed on the basis of a set of electrical measurements taken from a set of electrodes attached to the object boundary. Electric current is injected through electrodes, and the voltage produced on the object surface is recorded using several electrode pairs. Then an estimate of spatial distribution of conductivity (or its mutual resistivity) is computed. The possibility of ERT operation to monitor fibers, cracks, and moisture in concrete and other cement-based materials has been reported in previous studies. Hou and Lynch [11] applied ERT for detection of cracks in fiber reinforced cement composites loaded by axial cyclic loads and three-point bending. Karhunen et al. [12] demonstrated that ERT is able to detect diverse conductive and nonconductive inclusions in concrete. Hallaji et al. [13, 14] applied ERT for quantitative and qualitative imaging of damage detection in concrete and tracing moisture flow in cementitious materials.

Several computational methods, namely, finite element method (often termed the complete electrode model (CEM) in ERT), finite difference method, and boundary element method have widely been applied for modeling electric current flow to numerically solve governing physicallybased partial differential equation (PDE). However, the major difficulty of these traditional methods is their need to make a mesh in the solution domain or on its boundary, and consequently, their over-reliance on computational meshes. This hinders their application if the study domain is highly irregular and complex.

In order to overcome the difficulty mentioned above, mesh-free or meshless method was developed to establish a system of (linear) algebraic equations for entire domain of problem without creating pre-defined meshes. This method has mostly been used in hydraulic engineering problems in last two decades. Diverse types of meshless methods have been developed, like local Petrov-Galerkin [15], the boundary knot method, the kernel method, the H-p clouds method, and radial basis function (RBF)-related methods [16]. Among these meshless methods, RBF-related methods (Kansa's collocation method) [16] are the most interesting due to the following advantages [17]: 1) It doesn't require domain and boundary meshing; 2) there is no need for integration in domain and boundary; 3) point location is the only variable in RBF functions which makes it suitable for high dimensional problems; 4) RBF is easy to code and implement. A popular form of RBF is multiquadratic (MQ) function which was first applied by Hardy [18, 19] and later by Kansa [16] for the interpolation of scattered geographical data.

One challenging issue related to MQ-RBF method is the calibration of shape coefficient which is a case-sensitive parameter and will be discussed in section 3.1. The MQ interpolator performance strongly depends on the picked value of the shape coefficient. Kansa and Carlson [20] showed that interpolation accuracy can be improved by taking variable shape coefficient. Nourani and Mousavi [21] observed that the geometry of the problem and the governing PDE have important impact on shape coefficient in the MQ formulation whereas boundary condition has less effect. Golberg et al. [22] made use of statistical method of cross validation to determine the optimal shape coefficient. Bayesian approach is used in this paper to optimize shape coefficient.

Problems in ERT are classified into diffuse tomography modalities and ill-posed inverse problem. Ill-posed inverse problem solutions are severely sensitive even to a moderate error in modeling and measurement noise. In general, a valid solution of an inverse problem needs exact modeling of the measurements which leads to nonlinear equations. The traditional approach to inverse problem is to implement regularization methods [23]. Recently, Bayesian statistical approach has been used worldwide. In Bayesian framework, uncertainties like unknown conductivity distributions, shape coefficient and errors arising from differences between calculated and measured (observed) voltages are explicitly formulated with probability density functions (PDF). The explicit statistical models for the desired unknowns are called *prior*. For example, if the target inclusion inside concrete is a block of iron, the geometry of block would be the *prior* and the position of iron block should be determined. In this research, MQ-RBF is used in conjunction with Bayesian approach to calibrate shape coefficient and to reconstruct conductivity of domain by taking probable measurement noise into account in order to achieve an accurate model.

MQ-RBF is used to numerically solve differential equations of ERT formulation in two dimensions. Using Bayes' theorem, the related inverse problem changes to a statistical nonlinear problem in which the unknowns are the conductivity distribution and shape coefficient. In this study an experimental study is conducted to validate the proposed method. Accordingly, rectangle concrete samples were made and the electrical potential in different boundary nodes were measured. In order to solve the problem, Markov chain-Monte Carlo method (MCMC) [24–27] was used. Although computational cost of MCMC can apparently be high, by taking an

appropriate *prior*, results quickly converge. Furthermore, RBF has low computational cost which makes it suitable beside MCMC. MCMC methods belong to the class of algorithms which, for sampling from a PDF, depend on constructing a Markov chain that has a known distribution. Target accuracy improves as a function of the number of iterations.

In this paper, the ability of RBF meshless method in conjunction with Bayesian approach to simulate the electrical current flow in concrete are evaluated. It will be proven that RBF method are applicable in electrical tomography in order to find the location of inclusions inside concrete slab.

Section 2 introduces experimental setup and describes the preparation of slab sample as well as the tomography device which is used to inject electric current and measure potential through electrodes. Next, governing differential equation is introduced and meshless MQ-RBF method is presented in details. The bayesian theorem defined for ERT will be explained at the end of this section and a flowchart illustrates the proposed approach. The main results and conclusions are presented in sections 4 and 5, respectively.

## 2. MATERIALS AND METHODS

**2. 1. Experimental Setup** Electrical measurement of outer accessible surface of concrete is the first step for ERT. Then, concrete inclusion detection is done using numerical meshless method and statistical Bayesian rule. To do this, concrete slab samples with iron block inclusion, based on standards ASTM C136 (2006), ASTM C33 (1979) and ASTM C778 (2002) in dimension 16×12×3 cm were prepared. The dimension scaled for the slab is resembling the real floor pannel in construction. While casting, iron block in dimensions 2×2×1 cm were placed inside concrete in which most common Portland type II cement was used, and sand's FM was 2.9. The coarsest aggregate diameter was 10 mm which is one-third of slab thickness. Copper Electrode was attached to mold in order to inject electric current before casting (Figure 1).

Total number of electrodes to inject and measure electric current was 14 which were attached in an equal distance around concrete sample (Figure 1). Then, using tomography device, a 5 volt DC current was injected into a pair of electrodes via copper wires connected to electrodes. In this manner, one electrode gets zero volt potential (ground) and the other one gets 5 volt potential. Afterwards, the potential in the rest of electrodes which were charged due to electric field was measured. Figure 2 shows tomography device.

**2. 2. Governing Differential Equation** The governing differential equation simulating the electrical current flow and electrical potential distribution within the 2D domain is given as follows [28]:

$$\nabla.(\sigma\nabla u) = 0 \tag{1}$$

the following boundary conditions were applied:

$$\sigma(\vec{x})\frac{\partial u(\vec{x})}{\partial n} = 0\ \vec{x} \in \partial\Omega_1 \tag{2}$$

$$u(\vec{x}) = u_0(\vec{x})\ \vec{x} \in \partial\Omega_2 \tag{3}$$

where $\vec{x}$ indicates 2D coordinate vector $(x, y)$; $\sigma = \sigma(\vec{x})$ is the conductivity; $u = u(\vec{x})$ is the electric potential in the region $\Omega$; $\nabla$ is the differential operator; $\Omega$ is the current flow region; $\partial\Omega$ is the boundary region where $\partial\Omega_1$ implies electrode-free boundary and $\partial\Omega_2$ implies boundaries with electrodes$(\partial\Omega_1 \cup \partial\Omega_2 = \partial\Omega)$; $\partial/\partial n$ is the normal derivative; $n$ is an outward unit normal; $\sigma_0(\vec{x})$ is the potential measured through boundaries.

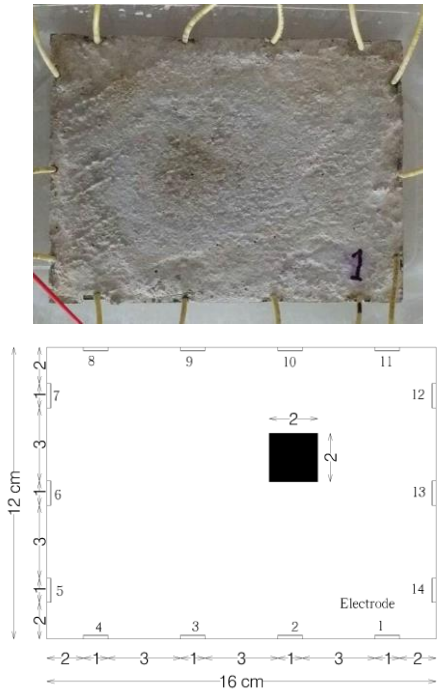


**Figure 1.** Concrete sample with electrodes in perimeter (Top) and schematic picture illustrates iron block location and electrode numbers (Bottom)

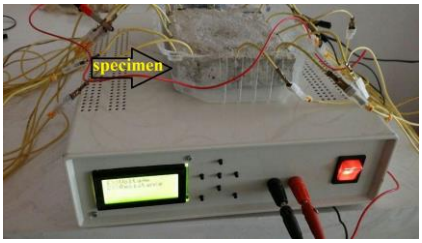


**Figure 2.** ERT measurement fixture; Tomography device and the specimen

The boundary condition (2) implies that there is no current flow through the electrode-free boundary outwards, and the boundary condition (3) indicates the amount of potential measured in electrode boundaries. It is worth noting that despite ignoring contact impedance between electrode and target surface, it is automatically modeled by calibrating and optimizing shape coefficient.

**2. 3. Meshless MQ-RBF Method for ERT** As discussed earlier, the RBF collocation technique is set up to solve PDEs which has been effectively applied in a wide range of engineering fields. The PDE of a general steady-state problem in d-dimension ($d = 1,2,3$) is as per the following equations:

$$Ru = f(\vec{x}) \text{ in } \Omega, \quad Bu = g(\vec{x}) \text{ on } \partial\Omega \tag{4}$$

where $u$ is the function (in this study, $u$ is potential), $R$and $B$are differential operators which are to be imposed to region ($\Omega$) and boundary ($\partial\Omega$) points of the computational domain, respectively. $\{P_i = (\vec{x}_i)\}_{i=1}^{N}$ indicates $N$ collocation nodes of the domain where, $\{(\vec{x}_i)\}_{i=1}^{N_I}$ are interior nodes, $\{(\vec{x}_i)\}_{i=N_I+1}^{N}$ are boundary nodes. Therefore, a solution for Equation (4) can be approximately written as follows [29]:

$$u(\vec{x}) = \sum_{j=1}^{N} h_j \, \Theta_j(\vec{x}) \tag{5}$$

where $\{h_j)\}_{j=1}^{N_I}$ are unknown coefficient vectors which will be calculated; and $\Theta_j(\vec{x}) = \Theta(\|P - P_j\|)$ denotes as radial based function (RBF). Here, $r = \|P - P_j\|$ represents the Euclidean distance between two nodes. The most commonly used RBF is multi-quadratic (MQ) function like $\Theta(r) = (r^2 + c^2)^m$ in which$m$ usually takes 0.5; $c$ is shape coefficient which is assumed constant in this study and will be optimized using Bayes' approach. By merging Equation (5) in Equation (4):

$$\sum_{j=1}^{N} R\left[\Theta_j(\vec{x}_i)\right]h_j = f(\vec{x}_i), \; i = 1,2,\dots,N_I \text{ for nodes inside the region} \tag{6}$$

$$\sum_{j=1}^{N} B\left[\Theta_j(\vec{x}_i)\right]h_j = g(\vec{x}_i), \; i = N_{I+1}, N_{I+1}, \dots, N \text{ for boundary nodes} \tag{7}$$

By solving the above simultaneous linear equations, coefficient vectors $\{h_i\}_{i=1}^{N}$ can be calculated at $\{(\vec{x}_i)\}_{i=1}^{N}$. By imposing MQ-RBF meshless Equations (6) and (7) on current flow Equations (1), (2), and (3), the following equation can be obtained for homogenous domains as an example:

$$\nabla^2\sigma = 0 \rightarrow \sum_{j=1}^{N} h_j \nabla^2\left[\Theta_j(\vec{x}_i)\right] = 0, \; i = 1,2,\dots,N_I \text{ for interior nodes} \tag{8}$$

$$\sum_{j=1}^{N} h_j \Theta_j(\vec{x}_i) = \sigma_0(\vec{x}_i) \quad i = N_{I+1}, N_{I+1}, \dots, N \text{ for boundary with electrode nodes} \tag{9}$$

$$\sum_{j=1}^{N} \frac{h_j \partial\Theta_j(\vec{x}_i)}{\partial n} = \vec{0} \quad i = N_{I+1}, N_{I+1}, \dots, N \text{ for electrode-free boundary nodes} \tag{10}$$

MQ function in the form of 2D is as follows [30]:

$$\Theta_j(\vec{x}) = \sqrt{(x - x_j)^2 + (y - y_j)^2 + c^2} \tag{11}$$

Afterward, by calculating $\{h_j)\}_{j=1}^{N_I}$, the approximate value for $u$at any point of $\vec{x}_i$ is

$$\hat{u}(\vec{x}) = \sum_{j=1}^{N} h_j \left[\sqrt{(x - x_j)^2 + (y - y_j)^2 + c^2}\right] \tag{12}$$

Then, Equations (8)-(10) can be expressed in the matrix form of:

$$\boldsymbol{U} = \boldsymbol{\Theta h} \tag{13}$$

where $\boldsymbol{U}$a vector whose arrays are either zero (right side of Equations (8) and (10)) or voltages measured from boundary with electrode (right side of Equation (9)), $\Theta_i(x_i)$ function of nodes$x_i$, and interpolation coefficient vector $h_i(i = 1{:}N)$ can be solved by simultaneous linear equations (Equation 13). Accordingly, Equation (12) can be utilized to evaluate the potential at interior nodes of the medium ($x_i$ for $i = 1,2,\dots,N_I$). By employing meshless technique, it is possible to calculate potential in all region given the conductivity distribution, which is in general called *forward problem* that has unique solution and is a mathematically well-behaved problem. However, the problem we encounter in this research is *inverse problem* which reconstructs the conductivity distribution given the boundary electric potential measurements and is a mathematically badbehaved problem.

If Equation (12) is Applied to electrode nodes, the same voltages will be obtained that were measured and used in Equation (13) beforehand, because the coefficient vector is computed via precise linear equations solution. In the same vein, it is impossible to regulate shape coefficient and verify the results. Therefore, in the proposed method, 50% of measured voltages were used for calibration and 50% for verification. Then, the difference between omitted voltages and real observed voltages can be determined:

$$\boldsymbol{U_0} = \widehat{\boldsymbol{U}} + \boldsymbol{e} \tag{14}$$

where $\boldsymbol{U_0}$ is observed voltages for verification and $\widehat{\boldsymbol{U}}$is corresponding estimated voltages using meshless method. It is clear that $\widehat{\boldsymbol{U}}$is a function of $c$ and$\sigma$, and their variations lead to change in$\widehat{\boldsymbol{U}}$. And$\boldsymbol{e}$ corresponds to noise vector.

**2. 4. Bayesian Theorem** A statistical approach for dealing with inverse problems is Bayes' theorem [31]:

$$\pi_{psr}(c, \sigma|u) = \frac{\pi(u|c,\sigma)\pi_{pr}(c,\sigma)}{\pi(u)} \tag{15}$$

where, $\pi_{pr}(c, \sigma)$ is the joint prior density function of shape coefficient $c$and conductivity vector $\sigma$, $\pi(u|c, \sigma)$ is likelihood density function of measured potential $u$ given unknown $c$and $\sigma$, $\pi(u)$ is marginal density function of potential which acts as a normalizer and is usually neglected, $\pi_{psr}(c, \sigma|u)$ is posterior density function of unknown$c$and $\sigma$, given measured potential $u$.

By neglecting $\pi(u)$, Equation (16) takes the following form:

$$\pi_{psr}(c,\sigma|u) \propto \pi(u|c,\sigma)\pi_{pr}(c,\sigma) \quad (16)$$

The likelihood density function $\pi(u|c,\sigma)$ is a conditional density of observations given the unknowns and thus describes the relation between the observation $u$ and unknown $\sigma$ and $c$. If it is assumed that $(c,\sigma)$ and $e$are mutually independent, the likelihood becomes [32]:

$$\pi(u|c,\sigma) = \pi_e(U_0 - \widehat{U}) \quad (17)$$

where $\pi_e$ is the probability function of the noise $e$. Additionally, if measured noise $e$ is considered as the normal distribution with zero mean and covariance $\Gamma_e$, the likelihood can be written:

$$\pi(u|c,\sigma) \propto exp\left(-\frac{1}{2}e^T\Gamma_e^{-1}e\right) \quad (18)$$

If $\sigma$ and $c$ are mutually independent, then:

$$\pi_{pr}(c,\sigma) = \pi(c)\pi(\sigma) \quad (19)$$

Also, if $\sigma$ and $c$ are assumed normal distribution with $\sigma^*$and $c^*$ mean and covariance $\Gamma_\sigma$ and $\Gamma_c$, respectively, prior density function can be written:

$$\pi_{pr}(c,\sigma) = exp\left(-\frac{1}{2}(c-c^*)^T\Gamma_c^{-1}(c-c^*)\right) * exp\left(-\frac{1}{2}(\sigma-\sigma^*)^T\Gamma_\sigma^{-1}(\sigma-\sigma^*)\right) \quad (20)$$

eventually posterior density takes the following form:

$$\pi(c,\sigma|U) \propto exp\begin{pmatrix} -\frac{1}{2}e^T\Gamma_e^{-1}e - \\ \frac{1}{2}(c-c^*)^T\Gamma_c^{-1}(c-c^*) - \\ \frac{1}{2}(\sigma-\sigma^*)^T\Gamma_\sigma^{-1}(\sigma-\sigma^*) \end{pmatrix} \quad (21)$$

Although solution of posterior density in Equation (22) is the real solution of statistical inverse problem, it is impractical and time-consuming in high dimensional problems. Some points are often estimated from posterior density. In this study, constant shape coefficient is applied in meshless method, therefore $c$ is a scalar. Maximum a posteriori (MAP) is the most widely used technique for estimation of statistical point:

$$(\sigma,c)_{MAP} = \underset{(\sigma,c)}{argmax}\pi(\sigma,c|U) \quad (22)$$

Equation (23) gives the most probable point of the posterior density. If the negative exponent is ignored in Equation (22), the problem is changed to minimization:

$$(\sigma,c)_{MAP} = \underset{(\sigma,c)}{argmin}F(\sigma,c|U) \quad (23)$$

where, Functional $F(\sigma,c;U)$ is of the form:

$$F(\sigma,c;U) = \frac{1}{2}\boldsymbol{e}^T\Gamma_{\boldsymbol{e}}^{-1}\boldsymbol{e} + \frac{1}{2}(\sigma-\sigma^*)^T\Gamma_\sigma^{-1}(\sigma-\sigma^*) + \frac{1}{2}(c-c^*)^T\Gamma_c^{-1}(c-c^*) = \|L_{\boldsymbol{e}}\boldsymbol{e}\|^2 + \|L_{\boldsymbol{\sigma}}\boldsymbol{\sigma}\|^2 + \left(\frac{c-c^*}{\sigma_c}\right)^2 \quad (24)$$

In Equation (24), $L_{\boldsymbol{e}}$ and $L_\sigma$are the upper triangular Cholesky factor of covariance matrices of noise and conductivity, respectively. Regarding the nonlinearity of Equation (24), computation of MAP estimation leads to nonlinear minimization.

Minimizers usually employ gradient-based iterative techniques. Considering the high dimensional problems, these methods do not necessarily converge. As an alternative way, Monte Carlo- Markov Chain (MCMC) technique can be utilized. Although MCMC is computationally expensive, the solution of Equation (24) would quickly converge in combination with the MQ-RBF method which is a low cost technique. MCMC has extensive applications and is used to solve the problem of sampling from a complicated distribution. Figure 3 shows the flowchart of the proposed meshless Bayesian model.

## 3. RESULTS AND DISCUSSION

In this research, meshless method, as an alternative numerical method, was employed to estimate electric potential in concrete with inclusions. To this end, concrete samples with iron block inclusion in different

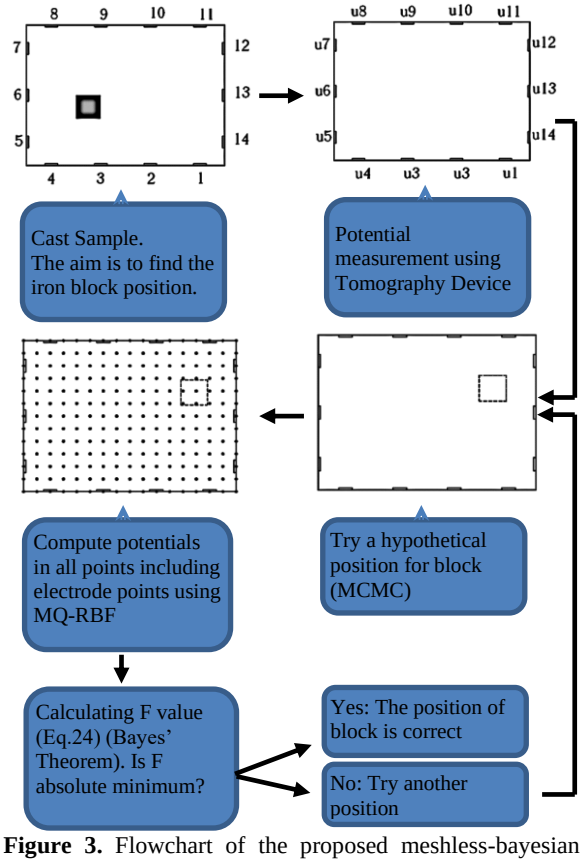


**Figure 3.** Flowchart of the proposed meshless-bayesian model

places were cast. Totally, 117 concrete samples were prepared. Later, DC current was injected via a pair of electrodes attached to the samples in different points, using tomography device. Next, electric potential was measured in all 14 electrodes. The number of pair electrode configurations for current injection was 35, out of which 7 configurations were pair electrodes opposite to each other, 14 pair electrodes adjacent to each other, and 14 pair electrodes in an alternate order. In every configuration, 7 electrode measurements were used for calibration of shape coefficient and the 7 remaining measurements were used for making noise vector and verification. In Table 1; configurations' number and corresponding pair electrodes are tabulated, in which the first electrode is ground connection with zero volt and the second one is charged with 5 volt.

In numerical modeling, measured voltages were employed in MQ-RBF model to estimate the potential in desired point of concrete sample where there was no measurement record. As an ability of MQ-RBF method for solving differential equation, both boundary conditions and internal condition can be utilized as the local boundary conditions. It is notable that the Kansa's [16] method accuracy depends on the determination of shape coefficient $c$ in MQ-RBF model (Equation (12)). Determination of $c$ is still an open question in the research field.

### 3. 1. The Optimum Value of Shape Coefficient

Hardy [18, 19] recommended that the value of $c$ be proportional to the mean distance of each data point to its nearest neighbor ($d_{ave}$), as $c = 0.815d_{ave}$. Golberg et al. [22] used statistical method of cross validation to determine the optimal shape parameter. Chen et al. [33] showed that in spite of appropriate ability of MQ-RBF modeling, choice of optimal $c$ relies on problem type and there is no specific mathematic theory to determine shape coefficient in diverse problems. Nourani et al. [34] made use of colony optimization algorithm as one of the optimization methods in engineering problems for solving differential equation in contaminant transport problems. They demonstrated that $c$ can vary based on physics and conditions of the problem. In this paper, statistical Bayesian method was used to optimize shape coefficient.

In the similar way, using Equation (24) regarding noise vector $\boldsymbol{e}$ and mean value of shape coefficient ($c^*$), optimal value of $c$ can be determined. Based on previous studies, primal value of $c^*$ which ranges between 0.1 and 4.0 was applied in Equation (24). According to Equation (24) in order to minimize function F, vector values $\boldsymbol{e}$ and $\boldsymbol{\sigma}$ and scalar value $c$ must be optimized. In other words, the aim of solving Equation (24) is to obtain the vector values of $\boldsymbol{e}$ and $\boldsymbol{\sigma}$ and scalar value of $c$ in order to make F the possible lowest value near zero. Monte Carlo method was used for this purpose. Based on the aforementioned explanations, the value of $c$ can efficiently change the output of Equation (24) in which the mean and variance of $c$ must be known. To this end, contour of optimized value of $c$ for different location of iron block and electrode configurations is depicted.

Figure 4 demonstrates the contour for electrode configurations 2, 15 and 26. In configuration 2 it is considerable that the $c$ mean value is 1.8 for all block locations, this means it is electrode configuration that is effective, and the location has no effect on the mean value. As a result, knowing that in configuration 2, maincurrent line between electrode 3 and 9 is far from concrete sample edge, it can be concluded that main current line distance from edge is one of the effective parameters in $c$ determination. On the other hand, as block approaches the center of sample, dispersion value of $c$ reduces so that maximum variance belongs to location (4, 3) and the minimum variance is related to (7, 5). In configuration 15, analogous to the configuration 2, mean value of $c$ is not affected by block location and equals 1.0; but, its dispersion is much lower than that of configuration 2 and generally is less than 0.03. Since the

**TABLE 1.** Configuration of pair electrodes used in current injection by tomography device

| Elect. Config. | | Number of Configuration | | | | | | |
|---|---|---|---|---|---|---|---|---|
| Opposite Pairs | Config. Number | 1 | 2 | 3 | 4 | 5 | 6 | 7 |
| | Pair Electrodes | 4,8 | 3,9 | 2,10 | 1,11 | 5,14 | 6,13 | 7,12 |
| Adjacent Pairs | Config. Number | 8 | 9 | 10 | 11 | 12 | 13 | 14 |
| | Pair Electrodes | 1,2 | 2,3 | 3,4 | 4,5 | 5,6 | 6,7 | 7,8 |
| | Config. Number | 15 | 16 | 17 | 18 | 19 | 20 | 21 |
| | Pair Electrodes | 8,9 | 9,10 | 10,11 | 11,12 | 12,13 | 13,14 | 14,1 |
| Alternate Pairs | Config. Number | 22 | 23 | 24 | 25 | 26 | 27 | 28 |
| | Pair Electrodes | 1,3 | 2,4 | 3,5 | 4,6 | 5,7 | 6,8 | 7,9 |
| | Config. Number | 29 | 30 | 31 | 32 | 33 | 34 | 35 |
| | Pair Electrodes | 8,10 | 9,12 | 10,12 | 11,13 | 12,14 | 13,1 | 14,2 |

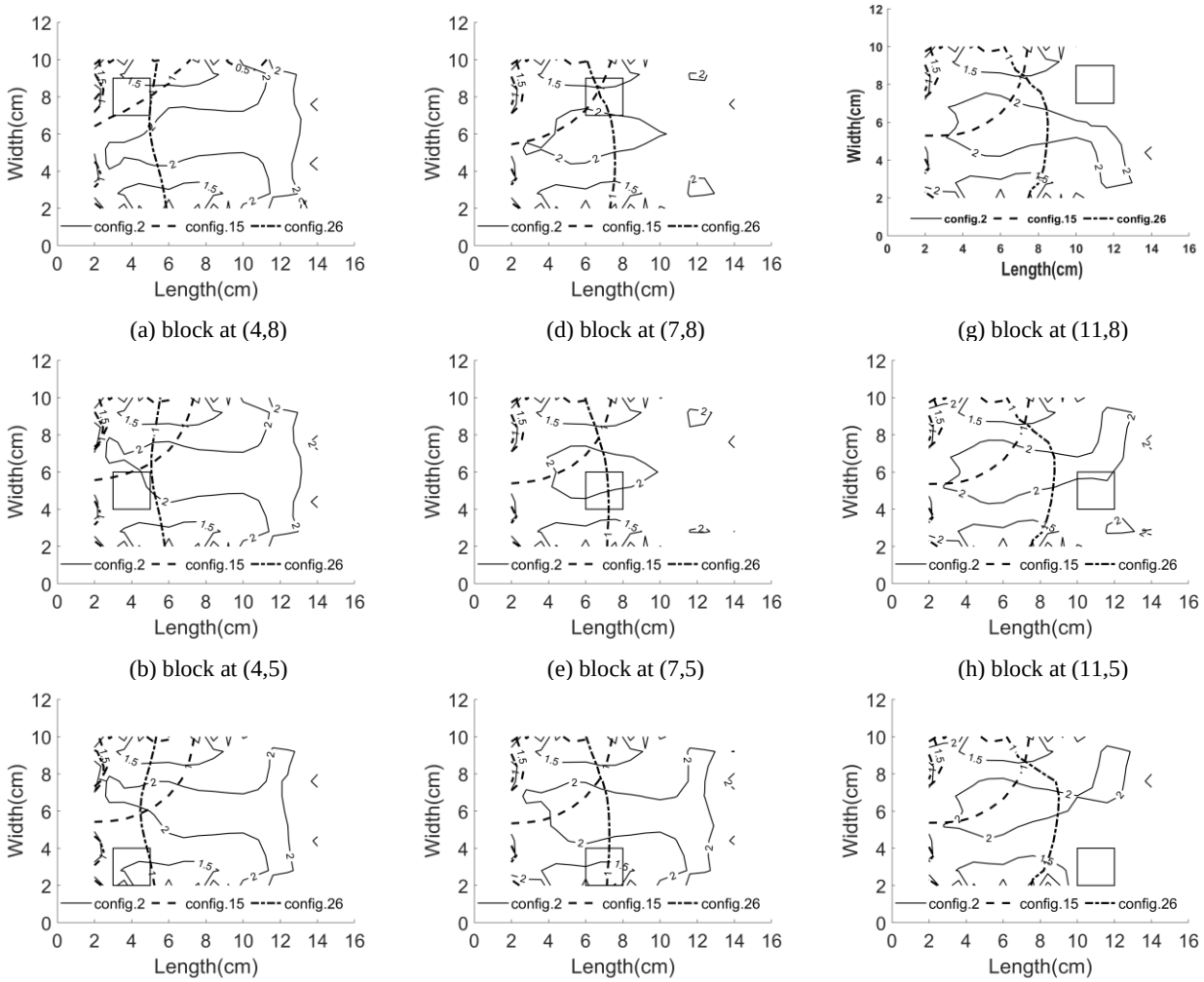


(a) block at (4,8) (d) block at (7,8) (g) block at (11,8)

(b) block at (4,5) (e) block at (7,5) (h) block at (11,5)

(c) block at (4,3) (f) block at (7,3) (i) block at (11,3)

**Figure 4.** Contour of shape coefficient for different block locations for configuration 2, 15 and 26. The square inside represents the block position.

main current line has the lowest distance from the edge, hence the more two electrodes get close together the less the mean value of *c* will be. In configuration 26. it is shown that mean value of *c* ranges from 0.9 to 1.1 and block location slightly influences the *c* in a way that as pair electrodes approach the iron block the mean value of *c* decreases. However, dispersion of *c* is 0.02 and lower than that of configuration 15.

For further assessment, optimized c value contour for opposite and alternate configurations of block location (5, 5) is depicted in Figure 5. From opposite configuration contour, it is found that for configurations close to the edge i.e. configurations 1, 4 and 5, the mean value of c is near 1.0 and the variance is low resembling adjacent and alternate configurations. In contrast, for configurations far from the edge i.e. 2, 4 and 6, the mean value is about 1.8 and its variance is increased.

For alternate configurations, results corroborate that by approaching main current line to the edge the mean value and variance of *c* decreases. The results of different block locations confirm the previous results. However, they are not presented here because of limited space. In general, when main current line is near the edge, mean value of *c* is 1.0 and when it is far from edge the mean value is 1.8. it is worthy to note that mean value and variances of *c* are considered as *prior* information and will be discussed in the next section. Low effect of block location in mean value of *c* is another outcome.

**3. 2. *e* and *c* Random Variables** According to Equations (18) and (20) ***e*** and *c* random variables are assumed normal distribution. Therefore, it is important to evaluate them for some cases. In Figure 6, ***e*** and *c* histogram and fitting normal distribution for configuration 2 is illustrated. Regarding this fact that the half of electrodes which used for verification are not random variables and the remaining electrodes are random variables and should be optimized, thereupon,

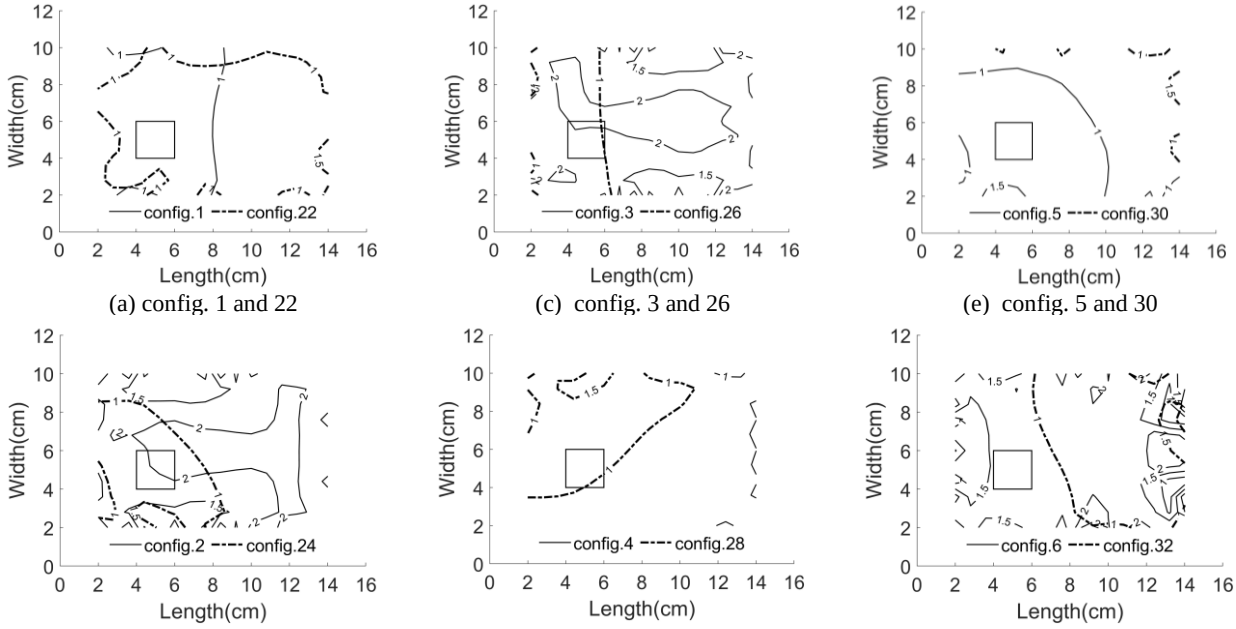


(a) config. 1 and 22 (c) config. 3 and 26 (e) config. 5 and 30

(b) config. 2 and 24 (d) config. 4 and 28 (f) config. 6 and 32

**Figure 5.** Contour of shape coefficient for block (5,5) for opposite and alternate configurations. The square inside represents the block position.

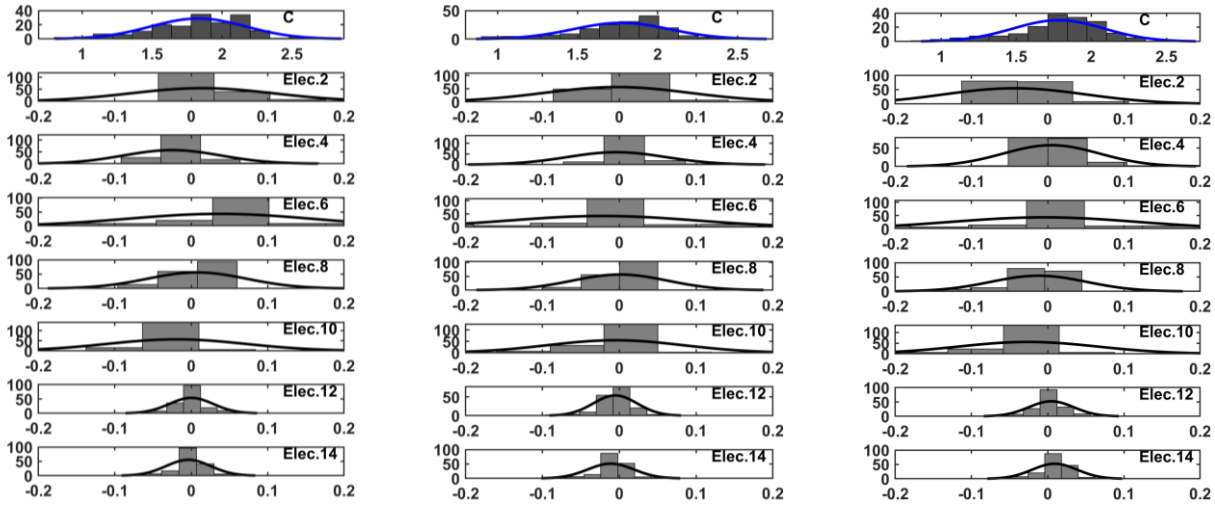


(a) block at (4,5) (b) block at (7,8) (c) block at (11,3)

**Figure 6.** histogram of random variables *c* and ***e*** for configuration 2. X axis represents the random variable value and Y-axis represents the number of iterations.

for maximum 7 number of electrodes histogram is demonstrated. it is remarkable that *c* distribution fits well with normal distribution so that it is fluctuated around the mean value discussed in former section and ranges between 0.5 and 2.5 which represents good dispersion. In ***e*** histogram it is shown that noise values are scattered around zero mean as expected and are generally in good agreement with normal distribution which influence tomography precision, because normal distribution assumption correctness which will be discussed in the following section has great impact on *likelihood* function.

Similarly, histogram of ***e*** and *c* for configuration 15 is plotted in Figure 7 which does not fit well with normal distribution. Dispersion is limited and variance is low. In accordance with Equation (24), low and zero variance value as denominator causes large calculation error and reduces tomography precision. On the other hand, histogram of ***e*** has good fitness with normal distribution, although in some electrodes fluctuation is not around

zero. Configuration 26 histograms show that although ***e*** is scattered around zero, it does not fit with normal distribution. It should be noted that ***e*** and *c* are random variables corresponding to *likelihood* and *prior* functions, respectively.

Furthermore, probabilistic tomography is possible with and without *prior*, but without *likelihood* it is not possible. So it is clear that conformity of assumptions for noise vectors ***e*** is more significant than shape coefficient *c*. Therefore, identification criterion for convenient configuration is greatly based on well-fitting of ***e*** for which results show the good ability of opposite configuration 2.

For comprehensive assessment, whole opposite configurations for block (5, 5) are illustrated in Figure 8. Results identify that ***e*** and *c* are in good agreement with normal distribution and ***e*** is scattered around zero means for all configurations whose main current line is far from the edge. Because of space limitations, histograms of remaining configuration are not presented here and only general conclusions are stated as follows: 1) Altering ranges of *c* for all configurations whose main current line is near the edge including opposite, adjacent and alternate configurations is between 0.8 and 1.4 and for main current line far from edge is between 0.5 and 2.5. 2) The longer the current line, the more random variables fit the normal distribution such as configuration 6 in proportion to configurations 2 and 3. 3) Iron block location has minor effect on distribution manner and values of random variables so this can make tomography difficult and ill-posed. 4) By approaching the electrodes to the main current line, noise values increase and the distributions become asymmetric.

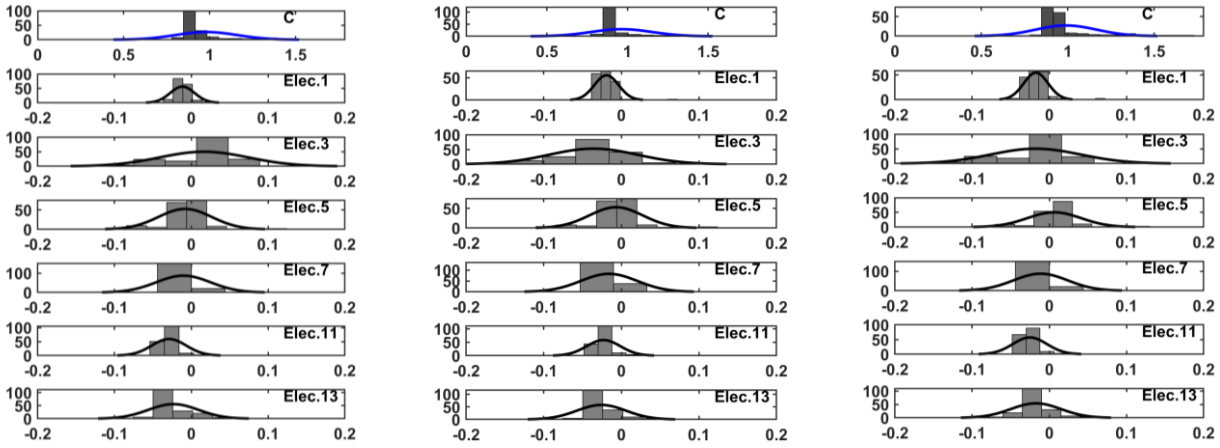


(a) block at (4,3) (b) block at (7,8) (c) block at (11,5)

**Figure 7.** histogram of random variables *c* and ***e*** for configuration 15. X axis represents the random variable value and Y-axis represents the number of iterations.

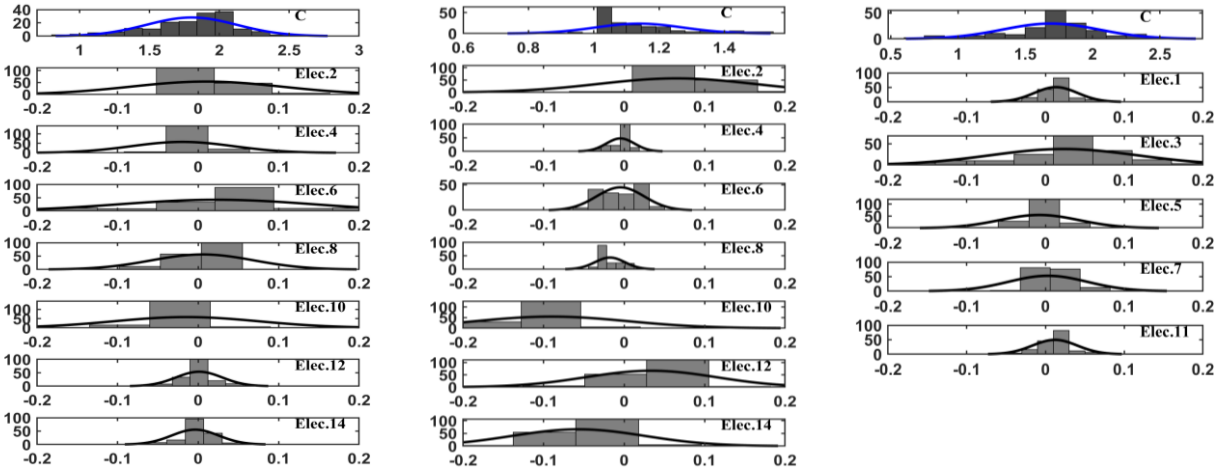


(a) config. 2 (b) config. 4 (c) config. 6

**Figure 8.** histogram of random variables c and ***e*** for block (5,5). X axis represents the random variable value and Y-axis represents the number of iterations.

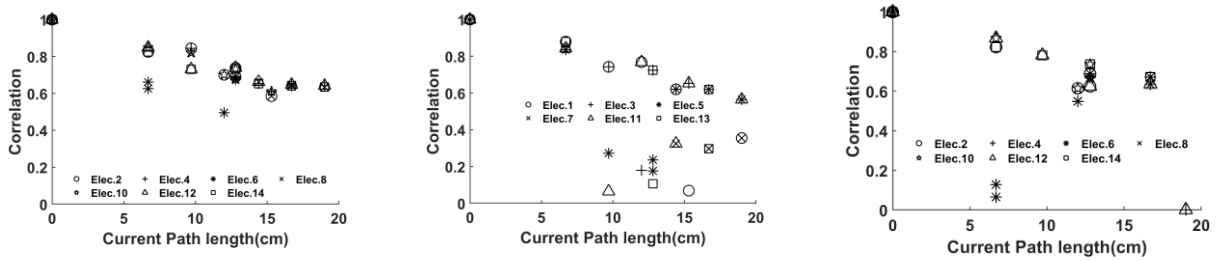


(a) config. 2 (b) config. 15 (c) config. 26

**Figure 9.** Correlation of electrodes versus current path length for configurations 2, 15 and 26 for block (7,5)

**3. 3. Covariance of Random Variables** One of the important advantages of probabilistic tomography is using distribution functions like multivariate normal distribution whose main parameters is covariance of random variables. Therefore, if in Equation (24) *prior* function is ignored and *likelihood* function is used merely (in some cases without having enough information, inevitably, it is impossible to make use *prior*) covariance is the only difference between probabilistic and deterministic tomography. In fact, covariance is linear relation among random variables and proper distribution of posterior can be obtained if this relationship is available. Hence, in this section relationship among random variables will be evaluated.

Figure 9 represents correlation between possible electric current path length of electrodes (not direct distance between electrodes) and noise values for each electrode with other 6 remaining electrodes for configuration 2, 15 and 26 for block (7, 5). In configuration 2, results show that there is a logical correlation between current path length and noise values; this means that by lengthening current path, correlation value decreases and vice versa. However, the least correlation value is 0.5 which reveals good linear relationship between electrodes.

Consequently, using linear regression, the relationship between current path length and noise values can be predicted. It is considerable that block location has trivial impact on correlation which is confirmable for configurations 15 and 26. In configurations 15 and 26, it can be seen that there is no clear relation between current path length and noise values and the covariance can't be predicted.

**3. 4. Probabilistic and Deterministic Tomography** As mentioned in previous sections, according to Equation (24) differences between classic tomography i.e. deterministic tomography and probabilistic tomography is *prior* function which is former knowledge from random variables $\boldsymbol{\sigma}$ and $c$ such as distribution manner and also $\boldsymbol{e}$ covariance value for *likelihood* function. In this section a comparison between deterministic and probabilistic tomography without *prior* function is done to make it clear that which one is superior in iron block detection using different configurations. It is worth noting that solo usage of configuration is not adequate for detecting the block location, and output of Equation (24) from various configuration should be combined in order to get the precise conclusion. Accordingly, one of the issues under study is to find the best combination of configurations to reach the goal. In Figure 10 deterministic and probabilistic tomography without *prior* for blocks (4, 3), (4, 5) and (4, 8) for combination of opposite, adjacent and alternate configurations 2, 15 and 26, are illustrated. The vertical axis displays the invert value of noise ($1 \div F(\sigma,c|U)$) and the horizontal axes show the plan of concrete sample. For location (4, 3) it is considered that probabilistic method has more accurate result than deterministic method, but for locations (4, 5) and (4, 8) results of both methods are satisfactory. It is emphasized that differences between two methods in this section is just covariance of noise values.

In Figure 11, tomography for block (9, 9) is shown with various configuration combinations. In picture (b) which is output of the combination of configurations 2 and 26, probabilistic method is satisfactory and precise compared to deterministic method (picture (a)). Picture (d) represents outputs from combination of alternate configurations 22, 24, 26, 28, 30, 32 and 34 which verifies accepted outcome of both methods. Picture (f) confirms high accuracy of probabilistic method using combo of opposite configurations 1, 2, 3, 4, 5, 6 and 7. Finally by merging output from pictures (d) and (f), exact conclusion can be gained for probabilistic method. Although doing tomography using combo from large number of configurations can cause to high precision results, it is obvious that it requires high calculation and time. Therefore the minimum number of configurations is considered.

Figure 12 demonstrates tomography for blocks (3,3) and (5,5) for combo of 1, 2, 3, 4, 5, 6 and 7 and validates the exactness of this combo. Generally, conclusions from this section can be summarized as follows: 1) Large number of configurations combo lead to high precision.

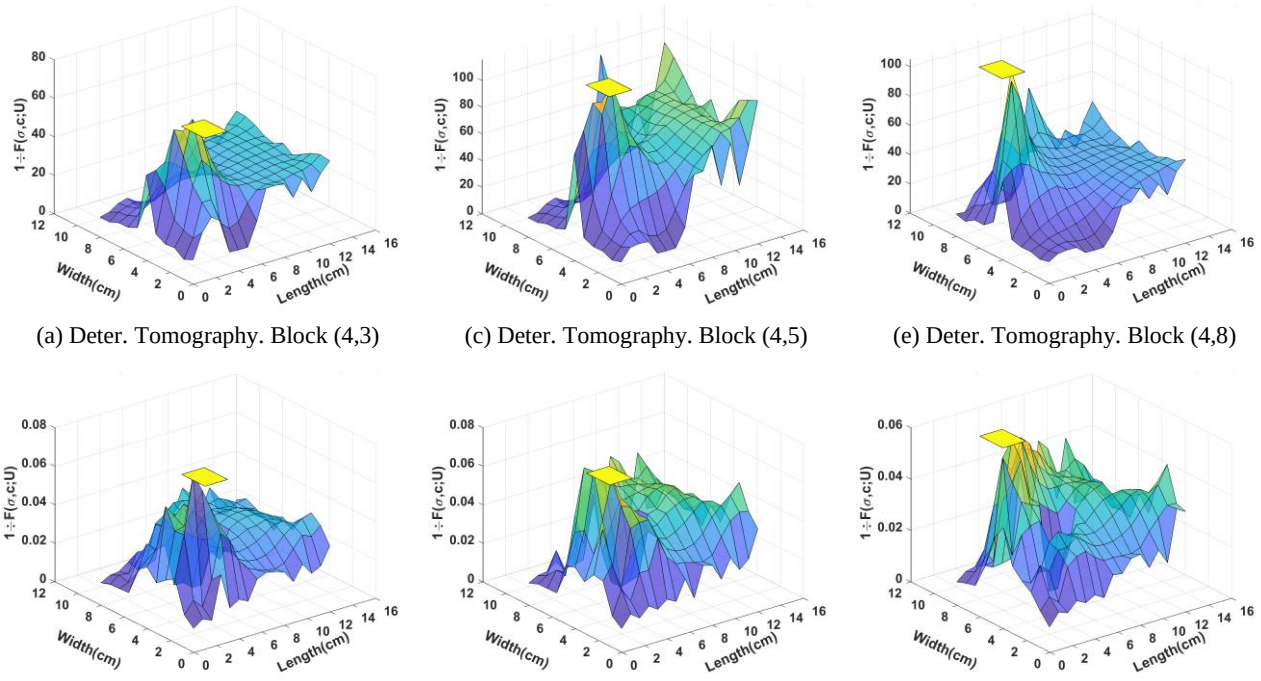


(a) Deter. Tomography. Block (4,3) (c) Deter. Tomography. Block (4,5) (e) Deter. Tomography. Block (4,8)

(b) Prob. Tomography. Block (4,3) (d) Prob. Tomography. Block (4,5) (f) Prob. Tomography. Block (4,8)

**Figure 10.** Deterministic and probabilistic Tomography map of blocks (4,3), (4,5) and (4,8) for combination of configuration 2, 15 and 26. The yellow square added to the map only represents the block position.

2) Combination of opposite configurations results in better outcomes than alternate ones, and combination of adjacent configurations generally fail. 3) Probabilistic method is more precise than deterministic method even without using *prior* functions. 4) The low cost combination is made from one opposite and one alternate configurations such as 2 and 26. Furthermore, the best combo is a combination from number of opposite and alternate configurations.

**3. 5. Probabilistic Tomography with *prior* Functions** Superiority of Bayes' theorem is in its use of former knowledge related to the problem which is called *prior*. Two *prior* functions mentioned above are $\boldsymbol{\sigma}$ and *c priors*. In order to use these functions it needs to know about vector $\boldsymbol{\sigma}$ and scalar *c* values. As discussed comprehensively in previous sections, it is feasible to gather statistical information about *c* e.g. mean and variance. But, it is generally not possible for $\boldsymbol{\sigma}$, unless approximate place of iron block is known. For further evaluations, in Figure 13, probabilistic tomography of iron blocks (3, 3), (5, 5) and (9, 9) are depicted for combination of configurations 2 and 3 in three cases: without *priors*, with *prior* function *c*, with *prior* function $\boldsymbol{\sigma}$. The results clearly proved that given prior information about the approximate location of block i.e. $\boldsymbol{\sigma}$ vector, tomography will be done with exact accuracy. In addition, results will improve with only *prior* function *c*.

## 4. SUMMARY

The aim of this study was to evaluate the possibility of meshless method to perform electrical tomography of concrete in order to detect iron inclusion. The electrical tomography enables to obtain conductivity of medium, i.e. σ in Equation (24). In meshless method, following the placement of a set of points on medium, σ vector is derived from the conductivity of corresponding points set up into a one-dimensional array. By optimizing and mapping σ vector, inclusions can be detected. For homogeneous material, the corresponding σ is vector of ones and has no role in Equation (1) and for heterogeneous material, σ vector plays the main role in Equation (1).

It should note that plain concrete is not homogeneous material due to pore and different sizes of aggregate. Also, concrete conductivity is only affected by moist cement paste and aggregate is not electrically conductive. However, provided that aggregates, cement paste and pores are distributed regularly, then concrete can be considered homogeneous which is not a practical condition and is of the uncertainty of the problem. Therefore, in numerical methods like finite element method, arrays of σ vector related to plain concrete domain cannot be assumed constant which causes large calculation costs and if it is assumed constant it causes calculation errors and leads to low accuracy. In contrast,

in meshless method, optimization of shape coefficient c makes it possible to take arrays of σ vector related to plain concrete domain constant without losing the accuracy. By this way, calculation speed will increase greatly.

In this research, it was shown that RBF approach is a proper conjugate for tomography of concrete to detect inclusions. Monte Carlo, as a minimizer, is used to find the optimum of σ to minimize F value in Equation (24). The main reason for this can be seen in Figures 10-13. It is obvious in some cases (for example Figure 12(b)) that there are multiple relative minimums in which most other minimizers are not able to find absolute minimum. Consequently, Monte Carlo in conjunction with meshless method result good outputs and can solve highly nonlinear problems. On the other hand, it is shown that to have a statistical problem, Bayesian theorem is an appropriate approach. This means that in classic approach, it is not feasible to use prior information in order to find maximum probability. Whereas, using Bayesian method, as proven in this paper, prior information from noise values, *c* value and approximate location of inclusion can be applied in model as covariance of noise value, c prior and σ prior, respectively.

As noticed before, shape coefficient used in this research is scalar and constant for entire domain and results became well. The advantage of scalar *c* is its easy application and optimization. To this point, optimum *c* for main current line near and far from the edge was

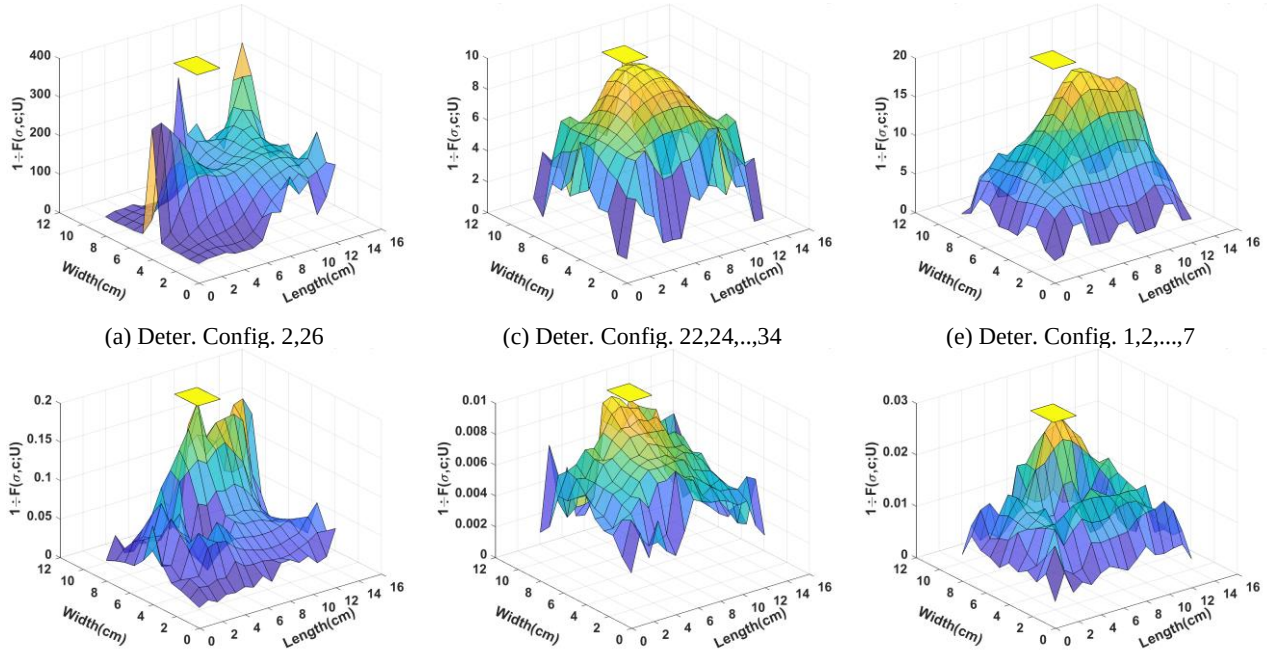


(a) Deter. Config. 2,26 (c) Deter. Config. 22,24,..,34 (e) Deter. Config. 1,2,...,7

(b) Prob. Config. 2,26 (d) Prob. Config. 22,24,..,34 (f) Prob. Config. 1,2,...,7

**Figure 11.** Deterministic and probabilistic tomography map of blocks (9,9) for combination of opposite and alternate congurations. The yellow square added to the map only represents the block position.

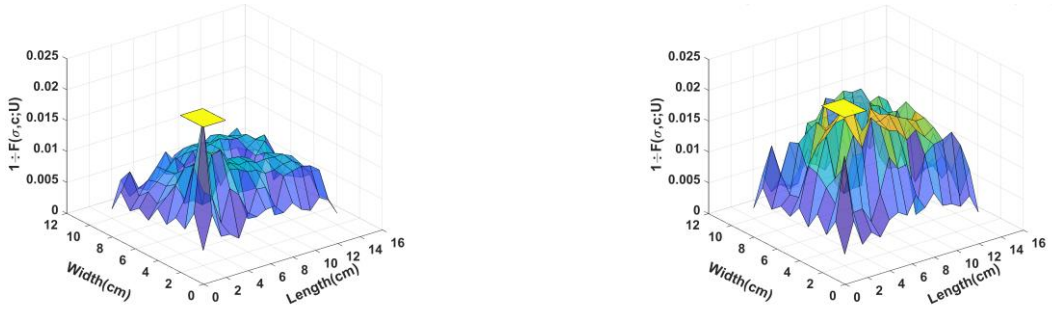


(a) Prob. Tomo. Block (3,3) (b) Prob. Tomo. Block (5,5)

**Figure 12.** Probabilistic Tomography map of blocks (3,3) and (5,5) for combination of all opposite configurations. The yellow square added to the map only represents the block position.

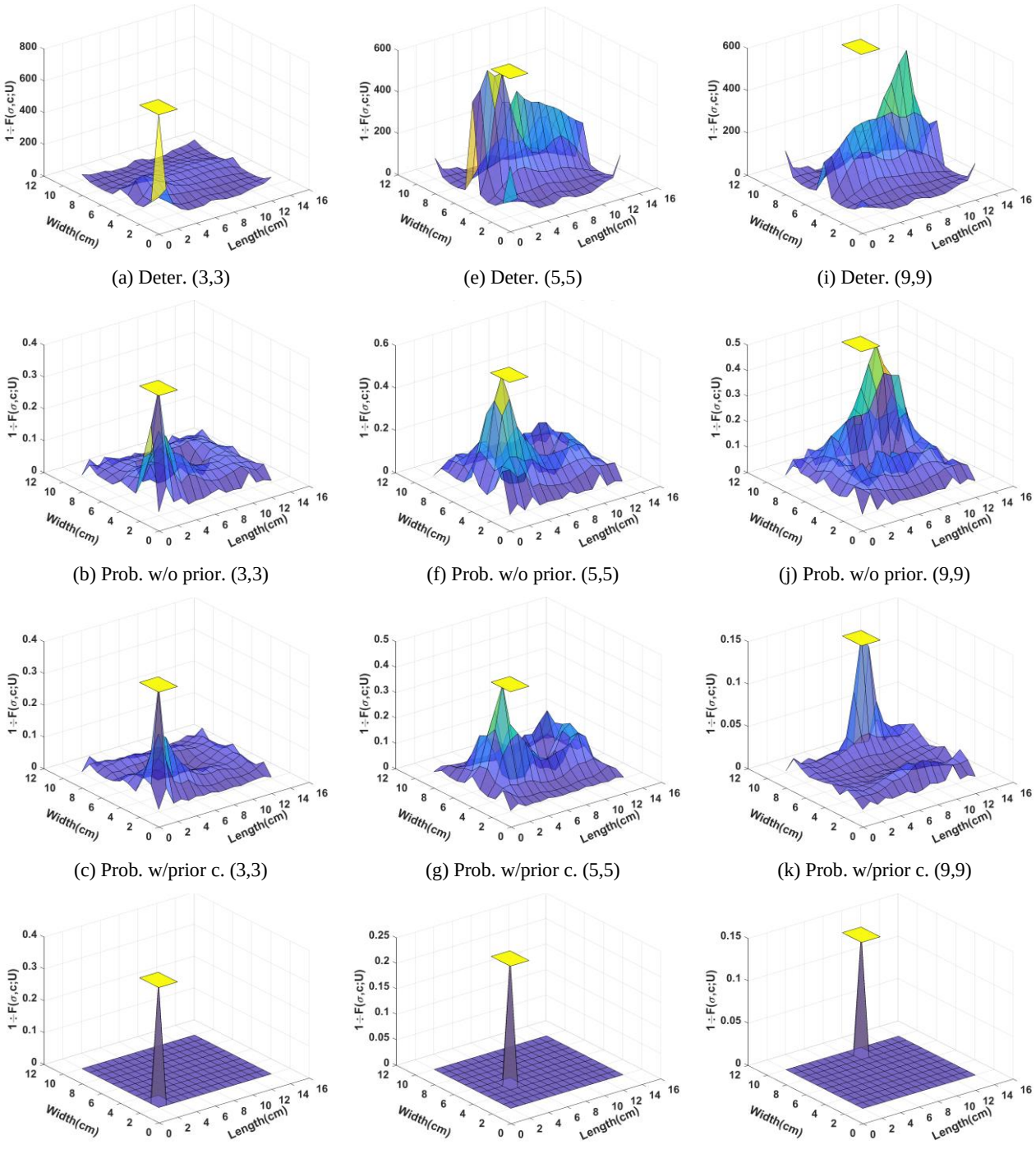


(a) Deter. (3,3) (e) Deter. (5,5) (i) Deter. (9,9)

(b) Prob. w/o prior. (3,3) (f) Prob. w/o prior. (5,5) (j) Prob. w/o prior. (9,9)

(c) Prob. w/prior c. (3,3) (g) Prob. w/prior c. (5,5) (k) Prob. w/prior c. (9,9)

(d) Prob. w/prior σ. (3,3) (h) Prob. w/prior σ. (5,5) (l) Prob. w/prior σ. (9,9)

**Figure 13.** Deterministic and probabilistic Tomography map of blocks (3,3), (5,5) and (9,9) for combination of configurations 2 and 3. The yellow square added to the map only represents the block position.

computed 1.0 and 1.8, respectively, which can be utilized in all cases without need to optimize repeatedly. In this way, calculation time was saved. However, the ability of variable $c$ or vector form of $c$ is left to future works. It is worth to note that RBF used in this study is of the form of MQ (Equation (11)) and two other common forms IMQ ($(r^2+c^2)^{-1/2}$) and Gaussian ($e^{-(r/c)^2}$) never resulted good conclusions, as expected. The reasoning would be: when the distance between two points increases, the influence of electrical potential to each other decreases which is involved in MQ function in contrast with IMQ and Gaussian.

## 5. CONCLUSION

The present paper combined numerical Multi-Quadratic Radial Based Function technique as a meshless method with statistical Bayesian rule to solve a two-dimensional differential equation which simulates electric potential distribution in concrete with inclusion. The proposed MQRBF model has some advantages including: there is no need for meshing, it is easy to use in high dimensions, it can solve the problems with incomplete or undetermined boundary conditions and complicated geometry. Thus, the proposed method is suggested here as an effective technique to solve the differential equation of electric potential distribution.

Results of this study indicated that shape coefficient in MQ-RBF model is significantly depended on boundary condition in a way that when main current line moves from the edge to the sample center, mean value of $c$ changes from 1.0 to 1.8, respectively. Also, range of $c$ for main current line near the edge is between 0.8 and 1.4 and for main current line far from the edge is between 0.5 and 2.5 in all configurations. Furthermore, in opposite configurations especially those whose main current line is long, distribution of random variable $c$ and $\boldsymbol{e}$ fits well with normal distribution, which is in agreement with the study assumption.

On the other hand, iron inclusion doesn't affect $c$ and $\boldsymbol{e}$ values and distribution manner very much, which makes using *prior* function difficult and results in an ill-posed problem. Noise covariance values play a key role in probabilistic tomography and possibility for estimating covariance matrix. The study shows that for opposite configurations, when current path is lengthened, correlation reduces almost linearly and becomes predictable. As expected, block location has minor effect on noise correlations. Results show that probabilistic method is more precise than deterministic method even without using *prior* functions. In order to obtain exact outputs, large number of configuration combinations is suggested. In total, opposite configuration combinations function well in detecting iron block location. Finally, tomography will end with best results if *prior* functions $\boldsymbol{\sigma}$ and $c$ are used.

## 6. REFERENCES


1. Salih, Y.A., Sabeeh, N.N., Yass, M.F., Ahmed, A.S. and Khudhur, E. S., "Concrete Beams Strengthened with Jute Fibers", ***Civil Engineering Journal***, Vol. 5, No. 4, (2019), 767–776.
2. Gao, Z. and Li, J., "Fuzzy analytic hierarchy process evaluation method in assessing corrosion damage of reinforced concrete bridges", ***Civil Engineering Journal***, Vol. 4, No. 4, (2018), 843–856.
3. Venkatesh, P. and Alapati, M., "Condition Assessment of Existing Concrete Building Using Non-Destructive Testing Methods for Effective Repair and Restoration-A Case Study", ***Civil Engineering Journal***, Vol. 3, No. 10, (2017), 841–855.
4. Shotorbani, A.R. and Saghai, H. R., "Modeling and implementing nonlinear equations in solid-state lasers for studying their performance", ***Emerging Science Journal***, Vol. 2, No. 2, (2018), 78–84.
5. Hansson, I.L.H. and Hansson, C. M., "Electrical resistivity measurements of Portland cement based materials", ***Cement and Concrete Research***, Vol. 13, No. 5, (1983), 675–683.
6. Ozyurt, N., Mason, T.O. and Shah, S. P., "Non-destructive monitoring of fiber orientation using AC-IS: An industrial-scale application", ***Cement and Concrete Research***, Vol. 36, No. 9, (2006), 1653–1660.
7. Woo, L.Y., Kidner, N.J., Wansom, S. and Mason, T. O., "Combined time domain reflectometry and AC-impedance spectroscopy of fiber-reinforced fresh-cement composites", ***Cement and Concrete Research***, Vol. 37, No. 1, (2007), 89–95.
8. Zhang, J., Monteiro, P.J., Morrison, H.F. and Mancio, M., "Noninvasive surface measurement of corrosion impedance of reinforcing bar in concrete—part 3: effect of geometry and material properties", ***Materials Journal***, Vol. 101, No. 4, (2004), 273–280.
9. Lataste, J.F., Sirieix, C., Breysse, D. and Frappa, M., "Electrical resistivity measurement applied to cracking assessment on reinforced concrete structures in civil engineering", ***Ndt & E International***, Vol. 36, No. 6, (2003), 383–394.
10. Wen, S. and Chung, D. D. L., "Electrical-resistance-based damage self-sensing in carbon fiber reinforced cement", ***Carbon***, Vol. 45, No. 4, (2007), 710–716.
11. Hou, T.C. and Lynch, J. P., "Electrical impedance tomographic methods for sensing strain fields and crack damage in cementitious structures", ***Journal of Intelligent Material Systems and Structures***, Vol. 20, No. 11, (2009), 1363–1379.
12. Karhunen, K., Seppänen, A., Lehikoinen, A., Monteiro, P.J. and Kaipio, J. P., "Electrical resistance tomography imaging of concrete", ***Cement and Concrete Research***, Vol. 40, No. 1, (2010), 137–145.
13. Hallaji, M. and Pour-Ghaz, M., "A new sensing skin for qualitative damage detection in concrete elements: Rapid difference imaging with electrical resistance tomography", ***NDT & E International***, Vol. 68, (2014), 13–21.
14. Hallaji, M., Seppänen, A. and Pour-Ghaz, M., "Electrical resistance tomography to monitor unsaturated moisture flow in cementitious materials", ***Cement and Concrete Research***, Vol. 69, (2015), 10–18.
15. Atluri, S.N., Kim, H.G. and Cho, J. Y., "A critical assessment of the truly meshless local Petrov-Galerkin (MLPG), and local boundary integral equation (LBIE) methods", ***Computational Mechanics***, Vol. 24, No. 5, (1999), 348–372.
16. Kansa, E. J., "Multiquadrics—A scattered data approximation scheme with applications to computational fluid-dynamics—II solutions to parabolic, hyperbolic and elliptic partial differential equations", ***Computers & Mathematics with Applications***, Vol. 19, No. 8–9, (1990), 147–161.
17. Nourani, V. and Babakhani, A., "Integration of artificial neural networks with radial basis function interpolation in earthfill dam seepage modeling", ***Journal of Computing in Civil Engineering***, Vol. 27, No. 2, (2013), 183–195.
18. Hardy, R. L., "Multiquadric equations of topography and other irregular surfaces", ***Journal of Geophysical Research***, Vol. 76, No. 8, (1971), 1905–1915.
19. Hardy, R. L., "Theory and applications of the multiquadric-biharmonic method 20 years of discovery 1968–1988", ***Computers & Mathematics with Applications***, Vol. 19, No. 8–9, (1990), 163–208.
20. Kansa, E.J. and Carlson, R. E., "Improved accuracy of multiquadric interpolation using variable shape parameters", ***Computers & Mathematics with Applications***, Vol. 24, No. 12,

(1992), 99–120.

21. Nourani, V. and Mousavi, S., "Spatiotemporal groundwater level modeling using hybrid artificial intelligence-meshless method", ***Journal of Hydrology***, Vol. 536, (2016), 10–25.
22. Golberg, M.A., Chen, C.S. and Karur, S. R., "Improved multiquadric approximation for partial differential equations", ***Engineering Analysis with Boundary Elements***, Vol. 18, No. 1, (1996), 9–17.
23. Tikhonov, A.N., Tikhonov, A. and TIKHONOV, A., "Solution of incorrectly formulated problems and the regularization method", ***Soviet Mathematics Doklady***, Vol. 4, (1963), 1035–1038.
24. Pouyan, A. and Yadollahzadeh Tabari, M., "Estimating reliability in mobile ad-hoc networks based on Monte Carlo simulation", ***International Journal of Engineering***, Vol. 7, No. 5, (2014), 739–746.
25. Zamankhan, P. and Montazeri, R., "Two and Three Dimensional Monte Carlo Simulation of Magnetite Nanoparticle Based Ferrofluids", ***International Journal of Engineering - Transaction A: Basics***, Vol. 26, No. 1, (2013), 99–104.
26. Tabatabaeian, Z.S. and Neshati, M. H., "Sensitivity Analysis of a Wideband Backward-wave Directional Coupler Using Neural Network and Monte Carlo Method (RESEARCH NOTE)", ***International Journal of Engineering - Transaction B: Applications***, Vol. 31, No. 5, (2018), 729–733.
27. Khodadadi, M., Kazemi, A. and Gorji, M., "Uncertainties due to fuel heating value and burner efficiency on performance functions of turbofan engines using monte carlo simulation", ***International Journal of Engineering - Transaction B: Applications***, Vol. 27, No. 7, (2014), 1139–1148.
28. Telford, W.M., Telford, W.M., Geldart, L.P., Sheriff, R.E. and Sheriff, R. E., "Applied geophysics", ***Cambridge university press***, (1990)
29. Li, J., Chen, C.S., Pepper, D. and Chen, Y., "Mesh-free method for groundwater modeling", ***WIT Transactions on Modelling and Simulation***, Vol. 32, (2002), 145–154.
30. Meenal, M. and Eldho, T. I., "Two-dimensional contaminant transport modeling using meshfree point collocation method (PCM)", ***Engineering Analysis with Boundary Elements***, Vol. 36, No. 4, (2912), 551–561.
31. Cowles, M. K., "Applied Bayesian statistics: with R and OpenBUGS examples", (Vol. 98), Springer Science & Business Media, (2013).
32. Melsa, J.L. and Cohn, D. L., "Decision and Estimation Theory", McGraw-Hill, (1978).
33. Chen, W., Fu, Z.J. and Chen, C. S., "Recent advances in radial basis function collocation methods", Heidelberg: Springer, (2014).
34. Nourani, V., Mousavi, S., Dabrowska, D. and Sadikoglu, F., "Conjunction of radial basis function interpolator and artificial intelligence models for time-space modeling of contaminant transport in porous media", ***Journal of Hydrology***, Vol. 548, (2017), 569–587.

## Persian Abstract

**چکیده**

تکنیک اندازه‌گیری پتانسیل الکتریکی (توموگرافی) به عنوان روش غیرمخرب برای ارزیابی ویژگی و دوام بتن مطرح شده است. در این مطالعه، روش عددی بدون شبکه برای حل معادله دیفرانسیل شبیه‌ساز توزیع پتانسیل الکتریکی در بتن با قطعه داخل آن به صورت دو بعدی مورد استفاده قرار گرفت. بدین منظور نمونه‌های بتنی با قطعه آهنی داخل آن در محل‌های مختلف آماده شد. سپس، از طریق جفت الکترودهای متصل به نمونه، جریان مستقیم به داخل بتن تزریق و پتانسیل الکتریکی در ١٤ الکترود واقع در پیرامون نمونه اندازه‌گیری شد. در مجموع ۳۵ آرایش جفت الکترودی مختلف برای تزریق جریان برنامه‌ریزی شد. قضیه بیزی جهت انجام توموگرافی احتمالاتی و نیز محاسبه ضریب شکل بهینه در روش عددی به کار رفت. نتایج این مطالعه مشخص می کند که ضریب شکل در مدل MQ-RBF مشخصاً وابسته به شرایط مرزی می‌باشد. همچنین، اگر طول جریان اصلی بلند باشد توزیع متغیرهای تصادفی $c$ و $e$ مطابقت خوبی با توزیع نرمال دارد که جزو فرضیات این مطالعه بود. بعلاوه، خروجی‌ها نشان داد که توموگرافی احتمالاتی حتی بدون استفاده از توابع پیشین دقیق‌تر از توموگرافی متعین می‌باشد. نتایج آزمایشگاهی نشان داد که مدل MQ-RBF عملکرد خوبی در توموگرافی الکتریکی دارد. این به دلیل وجود عدم قطعیت در ویژگی‌های فیزیکی بتن در شرایط واقعی است که قابل رفع وحل با استفاده از روش بدون شبکه از طریق بهینه‌سازی ضریب شکل می‌باشد.